Design and Modeling of a Hydraulically Amplified Magnetostrictive Actuator for Automotive Engine Mounts

Suryarghya Chakrabarti, Marcelo J. Dapino

Smart Vehicle Concepts Center, The Ohio State University, Columbus, OH, USA, 43210

ABSTRACT

A model is developed which describes the dynamic response of a Terfenol-D actuator with a hydraulic displacement amplification mechanism for use in active engine mounts. The model includes three main components: magnetic diffusion, Terfenol-D constitutive model, and mechanical actuator model. Eddy current losses are modeled as a one-dimensional magnetic field diffusion problem in cylindrical coordinates. The Jiles-Atherton model is used to describe the magnetization state of the Terfenol-D driver as a function of applied magnetic fields. A quadratic, single-valued model for the magnetostriction dependence on magnetization is utilized which provides an input to the mechanical model describing the system vibrations. Friction at the elastomeric seals is modeled using the LuGre friction model for lubricated contacts. The actuator's dynamic response is quantified in terms of the output displacement in the unloaded condition and force output in the loaded condition. The model is shown to accurately quantify the dynamic behavior of the actuator over the frequency range considered, from near dc to 500 Hz. An order analysis shows that the model also describes the higher harmonic content present in the measured responses. A study on the variation of energy delivered by the actuator with the load stiffness reveals that the actuator delivers the highest energy output near the stiffness match region.

Keywords: active powertrain mount, Terfenol-D actuator, magnetostrictive materials, hydraulic amplification, Jiles-Atherton model, LuGre friction model

1. INTRODUCTION

An engine mount is used to isolate engine vibrations from the passenger compartment and prevent excessive engine bounce from shock excitations. An active mount consists of a passive hydro-mount combined with an actuator which modulates the pressure of the hydraulic fluid so as to reduce its force transmissibility. Thus the performance of an active mount depends heavily on the performance of the actuator. Many electromagnetic actuators[1,2] have been suggested which offer improvements in the vibration isolation characteristics of the mounts. However, these actuators tend to exhibit a restricted frequency bandwidth, typically less than 80 Hz. To achieve broader frequency bandwidth, actuators using smart material drivers have been considered.[3,4]

Because smart materials capable of broadband response produce a stroke below mount requirements, the implementation of these materials in active mounts requires stroke amplification. Hydraulic amplification[5,6] is particularly attractive as it provides large mechanical gains in a restricted space. Ushijima and Kumakawa[3] developed a piezo-hydraulic actuator with a stroke of 70 μm which uses the hydraulic fluid in the mount for amplification. Shibayama et al.[4] developed a hydraulically amplified piezo actuator in which the hydraulic fluid used for amplification was separately sealed from the fluid in the mount. In these designs the mechanical performance is significantly lower than that predicted by linear mechanical models due to internal friction and compliances in the fluid chamber components. More advanced modeling is therefore required to accurately describe and analyze the behavior of hydraulically amplified actuators.

In this paper a dynamic model for the coupled response of a hydraulically amplified magnetostrictive actuator is presented. Losses due to internal friction, fluid chamber compliance, and support structure compliance are considered. The model is developed to describe the dynamic response of the hydraulically amplified Terfenol-D

Further author information: (Send correspondence to M.J.D)
S.C.: E-mail: chakrabarti.3@osu.edu, Telephone: 1-614-247-7480
M.J.D.: E-mail: dapino.1@osu.edu, Telephone: 1-614-688-3689

Industrial and Commercial Applications of Smart Structures Technologies 2010,
edited by M. Brett McMickell, Kevin M. Farinholt, Proc. of SPIE Vol. 7645,
76450G · © 2010 SPIE · CCC code: 0277-786X/10/$18 · doi: 10.1117/12.848875

actuator developed by Chakrabarti and Dapino,[7] with the primary intent of creating a tool for design optimization and control. The response of the cylindrical magnetostrictive driver to applied fields is modeled with a nonlinear and hysteretic description of magnetization as a function of magnetic field and bias stress based on the Jiles-Atherton model. The model is coupled with Maxwell's equations in order to quantify the radial dependence of magnetization and associated dynamic losses in the driver. A quadratic, single-valued model for the magnetostriction dependence on magnetization is utilized which provides an input to the mechanical vibratory model for the actuator. Friction at the elastomeric seals is described with the LuGre dynamic friction formulation, hence the model incorporates friction phenomena such as stick-slip, pre-sliding displacement, and the Stribeck effect.

A brief description of the actuator considered in this paper is provided in Section 2. The overall model structure is presented in Section 3 whereas Sections 4–6 respectively describe the three model components: magnetic diffusion, Terfenol-D constitutive model, and mechanical actuator model. A comparison of model results with experimental measurements is presented in Section 7.

2. ACTUATOR DESIGN

The actuator design is shown in Figure 1; further details can be found elsewhere.[7,8] The actuator has a fluid chamber with a large driving piston at one end and a small diameter driven piston at the other. The exact ratio of piston areas in this design is 69.6. The magnetic circuit consists of three Alnico ring magnets, a coil for generating dynamic fields, iron pieces for flux return, and a Terfenol-D rod. The permanent magnet provides the required magnetic bias to achieve bidirectional motion.

The mechanical preload on the Terfenol-D rod is created by a wave spring situated above the driven piston and by a disc spring located between the magnetic circuit and drive piston. The force produced by the wave spring on the rod is magnified by the fluid. One advantage of this configuration is that the fluid remains in compression during operation, thus reducing the chances of cavitation. The fluid is sealed on both ends by two dynamic o-rings.

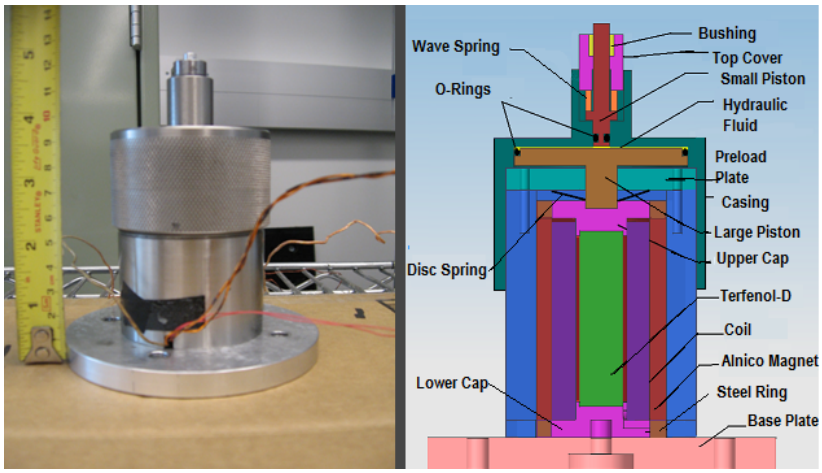

Figure 1. Physical actuator (left) and cutout (right).

3. MODEL APPROACH

Magnetostrictive materials deform when exposed to magnetic fields and change their magnetization state when stressed. Because these responses are nonlinear and hysteretic, developing comprehensive models that describe the coupled relationship between magnetic, elastic, and thermal phenomena in magnetostrictive materials has been a traditionally difficult problem. Numerous models exist which describe the strain-field loops at quasi-static frequencies. However, modeling the dynamic strain-field relationship in magnetostrictive transducers is a

much more challenging problem because of dynamic magnetic losses and vibration of the structural components. Dapino et al.[9] implemented a stress-dependent variation of the Jiles-Atherton model in combination with a quadratic magnetostriction model as an input to the wave equation describing the structural dynamics of a Terfenol-D transducer. Huang et al.[10] also implemented the Jiles-Atherton model but formulated a lumped parameter model to describe the structural dynamics and eddy currents. Another approach to model strain-field loops was developed by Sarawate and Dapino.[11] In this work, the radial dependence of field in a magnetostrictive rod is established by solving the diffusion equation; the resulting field is considered as an input to the constitutive model for the magnetostrictive rod. A similar modeling approach, shown in Figure 2), is followed in this paper. The principal difference lies in the way the averaging of the field is done and the complexity of the loading on the magnetostrictive rod. Sarawate and Dapino[11] calculated the average effective field by formulating a weighted sum of the field at different radii r while we consider $H(r,t)$ as an input to the Jiles-Atherton model to calculate the magnetization $M(r,t)$ and associated magnetostriction $\lambda(r,t)$. Averaging yields a bulk magnetostriction $\lambda_{avg}(t)$. The dynamic strain generated by the driver is obtained by coupling the magnetization model with the mechanical model.

In the work by Sarawate and Dapino[11] the mechanical load on the driver was a single degree-of-freedom linear spring, mass, and damper system which allows to resolve the magnetostriction waveform into Fourier components. The response of the mechanical system to those components was found analytically in the frequency domain. In the present work, the mechanical system consists of a hydraulic amplification mechanism with compliances and frictional losses at the seals. The resulting system thus has several types of nonlinearities. The complete system of equations is solved numerically and the Fourier components of the final periodic waveform are analyzed. Another important difference is the range of fields considered: Sarawate and Dapino[11] applied relatively low fields (16 kA/m pk-pk) to the Terfenol-D rod, resulting in reduced nonlinearity in the material response. In this work, the applied field is ≈ 55 KA/m pk-pk, which gives rise to increased nonlinearity and hysteresis in the magnetostrictive response.

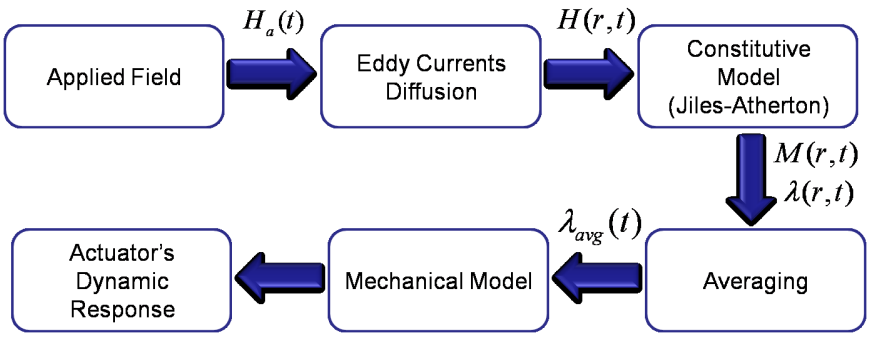

Figure 2. Flowchart for the actuator model.

4. MAGNETIC FIELD DIFFUSION

In an electro-magneto-mechanical system the electrical quantities – electric field **E**, electric flux density **D**, and current density **J** are coupled with the magnetic quantities – magnetic flux density **B** and magnetic field **H**. This coupling can be described with Ampére's law and the Faraday-Lenz law,

$$\nabla \times \mathbf{H} = \mathbf{J} + \frac{\partial \mathbf{D}}{\partial t}, \tag{1}$$

$$\nabla \times \mathbf{E} = -\frac{\partial \mathbf{B}}{\partial t}. \tag{2}$$

Ampére's law describes the generation of magnetic field due to a current density. The second term on the right hand side of (1) is known as displacement current and gives rise to electromagnetic radiation. This term can be neglected for the frequency range considered in this study. The Faraday-Lenz law describes the generation of an

electric field due to a changing flux density. The eddy current density associated with this field inside a material is $J = \sigma E$, where σ is the electrical conductivity of the medium (constant for ohmic materials). The direction of the eddy currents is such that the magnetic field they produce (through (1)) opposes the magnetic flux density change that induced them. Thus eddy currents impede alternating flux density. The effect of eddy currents is maximum near the center of an object exposed to alternating fields and gradually reduces to being negligible near the surface. This gives rise to a spatially variant magnetic field which can be obtained by combination of (1) and (2) into a single diffusion equation,

$$\begin{aligned} \nabla \times \nabla \times \mathbf{H} &= \nabla \times \mathbf{J} \\ &= \nabla \times (\sigma \mathbf{E}) \\ &= -\sigma \left(\frac{\partial \mathbf{B}}{\partial t} \right) \\ &= -\sigma \mu \left(\frac{\partial \mathbf{H}}{\partial t} \right), \end{aligned} \tag{3}$$

in which μ is the magnetic permeability of the material and the stress dependence of magnetic induction is assumed negligible. The left hand side of (3) can be simplified,

$$\begin{aligned} \nabla \times \nabla \times \mathbf{H} &= \nabla \left(\nabla \cdot \mathbf{H} \right) - \nabla^2 \mathbf{H} \\ &= \nabla \left(\nabla \cdot \mathbf{B} \frac{1}{\mu} \right) - \nabla^2 \mathbf{H} \\ &= -\nabla^2 \mathbf{H} \left(\because \nabla \cdot \mathbf{B} = 0 \right). \end{aligned} \tag{4}$$

For cylindrical geometries the magnetic diffusion equation takes the form

$$\frac{\partial^2 H}{\partial r^2} + \frac{1}{r} \frac{\partial H}{\partial r} = \sigma \mu \frac{\partial H}{\partial t}. \tag{5}$$

The boundary condition at the surface of the rod for a harmonic applied field is $H(R,t) = H_0 e^{i\omega t}$. We assume the solution to have the form $H_0 \tilde{h}(r) e^{i\omega t}$ with $\tilde{h}(r)$ a complex function. Equation (5) then reduces to

$$\frac{\partial^2 \tilde{h}}{\partial r^2} + \frac{1}{r} \frac{\partial \tilde{h}}{\partial r} - i\sigma\mu\omega\tilde{h} = 0. \tag{6}$$

Assuming μ to be constant over the range of applied fields, the solution to (6) can be written as done by Knoepfel,[12]

$$\tilde{h}(r) = \frac{I_0(q(r))}{I_0(q(R))}, \tag{7}$$

where I_0 is the modified Bessel function of order zero, $q(r) = \left(\sqrt{i\sigma\mu\omega} \right) r$, and R is the radius of the magnetostrictive rod. Figure 3 shows the magnetic field in the magnetostrictive rod as a function of r at 500 Hz for $\mu = 5\mu_0$ and $1/\sigma = 58e-8$ Ωm. The field at the center of the rod is smaller in magnitude and lags behind the field on the surface.

5. JILES-ATHERTON EQUATIONS

The Jiles-Atherton model[13] is implemented here to describe the magnetization in the magnetostrictive rod as a function of applied magnetic fields. The basic governing equations of the model are described here. The total magnetization at any instant of time can be written as a combination of an anhysteretic and an irreversible component,

$$M = cM_{an} + (1-c)M_{irr}. \tag{8}$$

Here, c is a reversibility parameter which accounts for reversible bowing of domain walls. When $c = 1$, domain wall motion is completely reversible and when $c = 0$, domain wall motion is completely irreversible. The anhysteretic magnetization is given by the Langevin function as

$$M_{an} = M_s \left(\coth \left(\frac{H_e}{a} \right) - \left(\frac{a}{H_e} \right) \right), \tag{9}$$

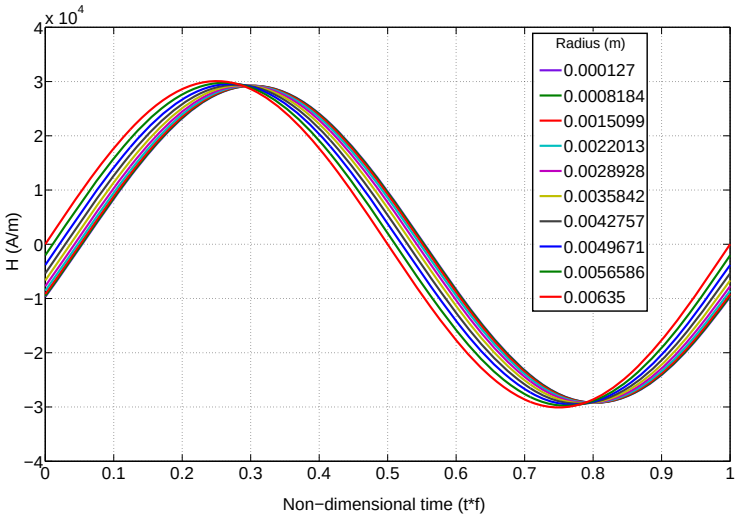

Figure 3. Field at 10 discrete radii from $r = 0.127$ mm to $r = 6.35$ mm.

where a is a shape parameter which controls the slope of the anhysteretic magnetization curve, M_s is the saturation magnetization of the material, and H_e is an effective magnetic field. In the original Jiles-Atherton model, H_e is a mean field that accounts for Weiss-type interactions. We use the formulation for H_e proposed by Dapino et al.,[14] which includes a Weiss-type mean field with parameter α and an effective field due to bias stresses σ_{bias},

$$H_e = H + \underbrace{\left(\alpha + \frac{9}{2}\frac{\sigma_{bias}\lambda_s}{\mu_0 M_s^2}\right)}_{\tilde{\alpha}} M. \tag{10}$$

The derivative of the total magnetization with respect to the applied field can be written as

$$\begin{aligned}\frac{dM}{dH} &= c\frac{dM_{an}}{dH} + (1-c)\frac{dM_{irr}}{dH} \\ &= c\frac{dM_{an}}{dH_e}\left(\frac{dH_e}{dH}\right) + (1-c)\frac{dM_{irr}}{dH_e}\left(\frac{dH_e}{dH}\right),\end{aligned} \tag{11}$$

where

$$\frac{dH_e}{dH} = 1 + \tilde{\alpha}\frac{dM}{dH}. \tag{12}$$

The irreversible magnetization is calculated through a law of approach to the anhysteretic magnetization,

$$\frac{dM_{irr}}{dH_e} = \frac{M_{an} - M_{irr}}{\delta k}, \tag{13}$$

where k is a parameter that quantifies the average energy required to break pinning sites and δ is dimensionless variable which is $+1$ for increasing fields and -1 for reducing fields. The derivative of the anhysteretic magnetization relative to the effective field is

$$\frac{dM_{an}}{dH_e} = \frac{M_s}{a}\left(-\left(\frac{1}{\sinh\left(\frac{H_e}{a}\right)}\right)^2 + \left(\frac{a}{H_e}\right)^2\right), \tag{14}$$

Recognizing that the field is radially dependent, combination of (11)-(14) yields a single expression for the variation of $M(r)$ with respect to $H(r)$,

$$\frac{dM}{dH}(r) = \underbrace{\left[c\frac{dM_{an}}{dH_e}(r) + \frac{M_{an}(r) - M(r)}{\delta(r)k}\right]}_{\Phi_{(M(r))}} \left[1 + \tilde{\alpha}\frac{dM}{dH}(r)\right], \tag{15}$$

which can be rearranged to give

$$\frac{dM}{dH}(r) = \left(\frac{\Phi_{(M(r))}}{1 - \tilde{\alpha}\Phi_{(M(r))}}\right). \tag{16}$$

Assuming the prestress is sufficiently large, the magnetostriction can be approximately modeled as a single valued function of magnetization through the relation

$$\lambda(r) = \frac{3}{2}\frac{\lambda_s}{M_s^2}M(r)^2. \tag{17}$$

An average magnetostriction is obtained through a weighted sum over the cross-section of the rod,

$$\lambda_{avg} = \frac{1}{\sum_{i=1}^{n} N(r_i)} \sum_{i=1}^{n} \lambda(r_i)N(r_i), \tag{18}$$

where r_i are the discrete radii at which the magnetostriction is evaluated and $N(r_i)$ are the weights. Figure 4 shows how the average magnetostriction decreases and becomes delayed with increasing actuation frequency. Table 5 lists the values of the Jiles-Atherton model parameters used in the calculations.

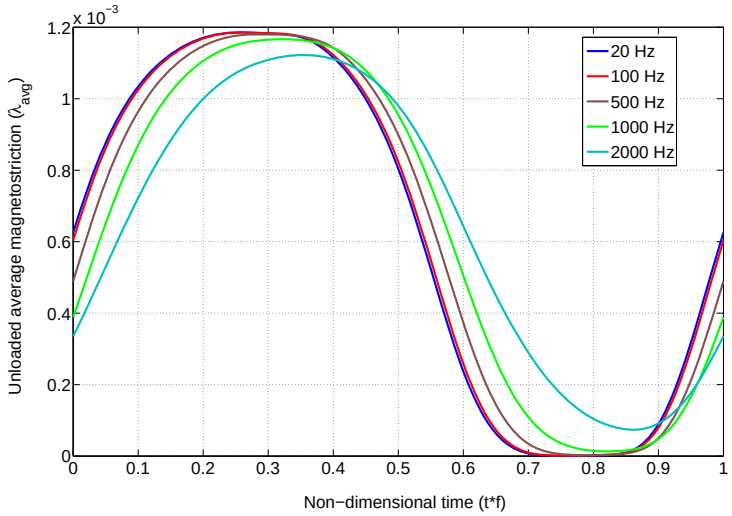

Figure 4. λ_{avg} at different frequencies.

6. MECHANICAL MODEL

A mechanical model for the hydraulically-amplified actuator is shown in Figure 5. The pressure variation in the fluid can be linearized for small volumetric changes as follows,

$$\Delta p = \beta\frac{\Delta V}{V_{ref}}, \tag{19}$$

where β is the fluid bulk modulus and V_{ref} is the fluid volume employed to achieve amplification. Volume change ΔV can be written in terms of the piston displacements x_L and x_p, the corresponding piston cross-sectional areas

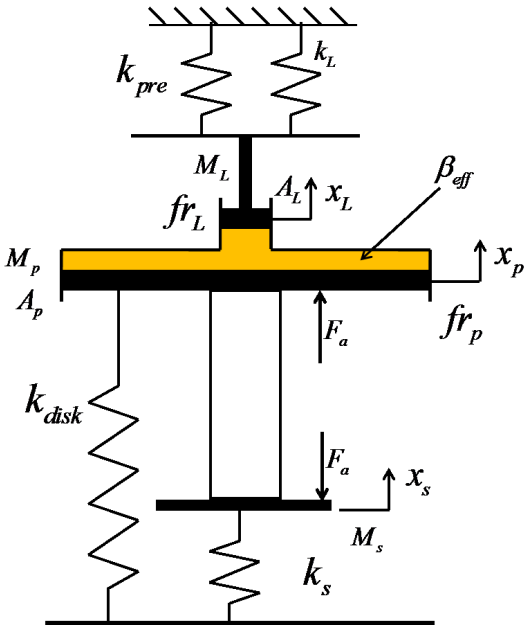

Figure 5. Schematic representation of the actuator's mechanical model.

A_L and A_p and the volumetric displacement of the fluid chamber components written in terms of the change in chamber pressure Δp and their stiffness C_o as

$$\Delta V = A_p x_p - A_L x_L - \frac{\Delta p}{C_o}. \tag{20}$$

Combination of (19) and (20) gives

$$\Delta p = \underbrace{\left(\frac{C_o \beta}{C_o V_{ref} + \beta}\right)}_{\beta_{eff}} (A_p x_p - A_L x_L). \tag{21}$$

Parameter β_{eff} is an effective modulus which quantifies the compliance of the fluid and different fluid chamber components including the o-rings, pistons, and casing. The fundamental deformation equation that must be satisfied by the magnetostrictive rod at all times is

$$\lambda_{avg} - \frac{\sigma_c}{E} = \epsilon = \frac{x_p - x_s}{l_a}, \tag{22}$$

which states that the total strain in the rod having modulus E is a superposition of the average magnetostriction and the strain induced by compressive stress (σ_c). The force generated by the Terfenol-D rod having a cross-sectional area A_r is

$$F_a = \sigma_c A_r = E A_r \lambda_{avg} - \frac{E A_r}{l_a}(x_p - x_s). \tag{23}$$

Table 1. Jiles-Atherton parameter values.

Parameter	Value	Parameter	Value
E (GPa)	32	a (A/m)	6512
c	0.18	α	0.046
k (A/m)	3000	λ_s	1150
σ_{bias} (ksi)	-1.0	M_s (A/m)	7.65×10^5

The equations of motion for the two pistons and the support structure are

$$M_p\ddot{x_p} + (k_{disk})\, x_p + fr_p = -\Delta p A_p - \sigma_c A_r, \tag{24}$$

$$M_L\ddot{x_L} + (k_L + k_{pre})x_L + fr_L = \Delta p A_L, \tag{25}$$

$$M_s\ddot{x_s} + k_s x_s = -F_a, \tag{26}$$

where k_L and k_{pre} are the stiffness of the load and preload springs acting on the driven piston, k_{disk} is the stiffness of the disk spring acting on the Terfenol-D rod, fr_L and fr_p respectively denote the friction forces at the small and large piston. Friction at the smaller piston seal has a significant impact on the dynamic response of the actuator since actuation forces are low and velocities are high at this end. Actuation forces at the larger piston are high, hence a small frictional force would not have much effect on the dynamic response of the transducer. For this reason, it is essential to accurately quantify the friction dynamics at the smaller piston. The LuGre model for lubricated contacts[15] is used to model the frictional force based on the bristle interpretation of friction. The LuGre model equations are given by

$$\begin{aligned} &\frac{dz}{dt} = v - \sigma_0 \frac{|v|}{g(v)} z, \\ &g(v) = F_c + (F_s - F_c)e^{-(v/v_s)^2}, \\ &F_r = \sigma_0 z + \sigma_1(v)\frac{dz}{dt} + \sigma_2 v. \end{aligned} \tag{27}$$

Here, z is the bristle deflection state, F_s and F_c are the static and Coloumb frictional forces, σ_0, σ_1, σ_2 are the bristle stiffness, bristle damping and viscous damping coefficients respectively, and v_s is the Stribeck velocity. The LuGre model parameters are provided in Table 2.

Table 2. Parameter values for the friction model.

Parameter	Driven Piston(small)	Driver Piston (large)
σ_0 (N/m)	0.34×10^5	1×10^7
σ_1 (Ns/m)	35	0
σ_2 (Ns/m)	4.3	5×10^4
v_s (m/s)	0.0009	0.0009
F_c (N)	5.2 (for $v > 0$)	100
	11.0 (for $v < 0$)	
F_s (N)	5.8 (for $v > 0$)	120
	11.1 (for $v < 0$)	

7. MODEL RESULTS

7.1 Mechanically unloaded tests

The actuator was run at discrete frequencies from 10 Hz to 500 Hz with a mechanical prestress of $\approx$ 1 ksi (6.9 MPa) acting on the Terfenol-D rod. No external loading spring is used. The Terfenol-D rod is magnetically biased by an Alnico magnet with a field of $\approx$ 27 KA/m. The actuator is driven with a 4.5 A sinusoidal current with no d.c bias. The strain on the surface of the Terfenol-D rod is measured with a strain gage and the displacement of the pushrod is measured with a laser displacement sensor. Figure 6 shows the experimental and modeled time domain responses of the pushrod displacement at varied actuation frequencies. The model describes the initial hysteresis and the nonlinear shape of the response at low actuation frequencies. The hysteresis comes largely from the frictional forces in the seals and partly from the material behavior causing a delay in the device response. As the actuation frequency increases, inertia and damping cause additional time lag and the associated phase lag causes a CCW rotation of the loop. A Fourier analysis on the experimental and modeled responses is carried out and the spectral content of the waveforms are compared at different frequencies. Figure 7 shows the

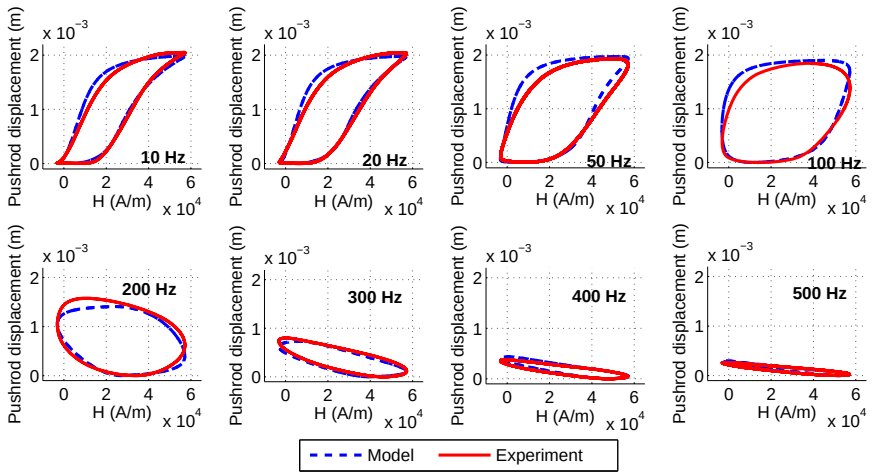

Figure 6. Output pushrod displacement-field loops at different actuation frequencies.

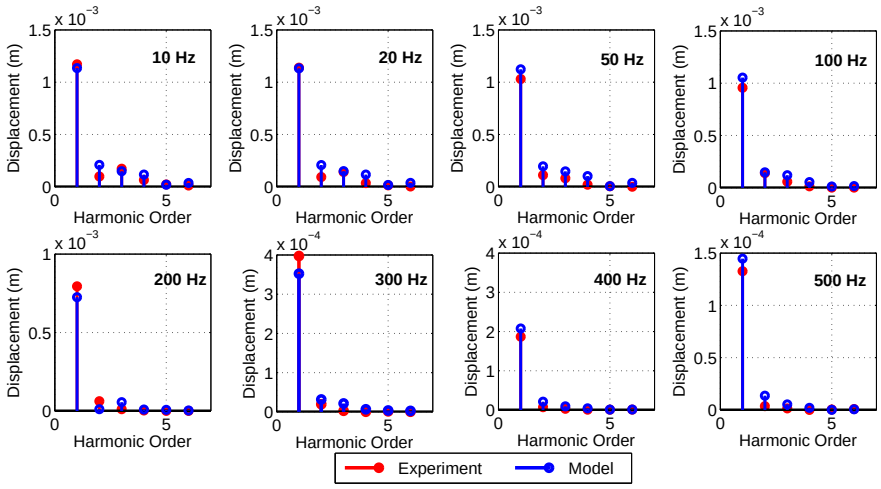

Figure 7. Output pushrod displacement orders.

Fourier components of the response. The model describes the trends in the higher order components. Figure 8 shows the magnitude and phase of the first order component of the pushrod displacement. Strong correlation is obtained in the pushrod displacement response in both magnitude and phase.

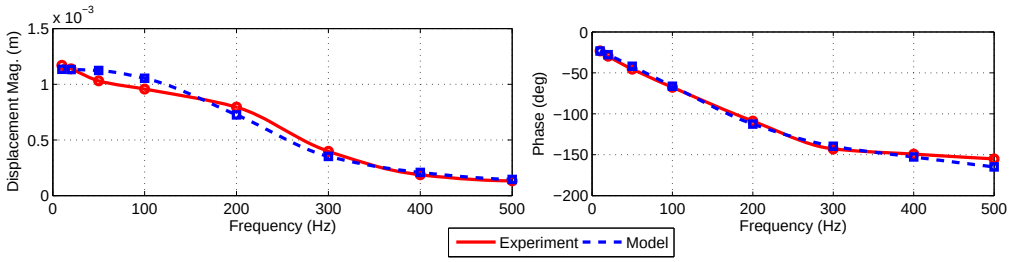

Figure 8. Output pushrod displacement magnitude and phase (first order).

7.2 Mechanically loaded tests

To obtain a measure of the actuator's performance under load, the setup shown in Figure 9 is employed. The pushrod compresses a wave spring and the force generated by the spring compression is measured with a load cell. The springs work only under compression while the Terfenol-D actuator produces bidirectional output. To ensure that the springs always remain in compression, they need to be pre-compressed using a height adjustor. Each spring is compressed until it creates a force of 8 N. This additional load combined with the weight of the other components attached to the pushrod is amplified through the fluid and creates an additional prestress of ≈ 1 ksi on the Terfenol-D rod. Thus the value of the parameter σ_{bias} was changed to 2 ksi (13.8 MPa) for these calculations. All of the other parameters are kept the same for both the unloaded and loaded conditions. In addition the external loading springs were found to have some non-linearity in their response and a mean stiffness was computed based on the range of forces generated by the Terfenol-D actuator. Figure 10 shows the force produced by the actuator when loaded with springs of different stiffnesses and driven at 5 Hz. The force-field

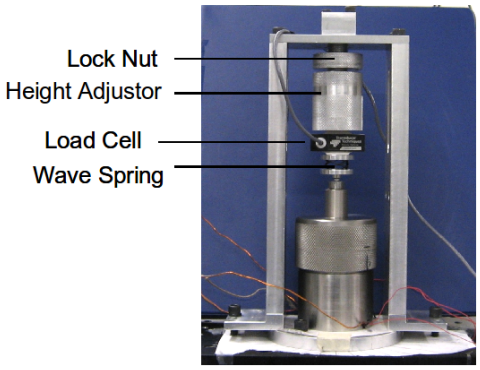

Figure 9. Setup used to test actuator performance under spring loads.

loops are not as accurate as the displacement-field loops obtained for the unloaded condition. The model over-predicts the hysteresis in the loops. This could be because loading the pushrod with external components might have altered the friction forces in ways not incorporated in the model. Also, the force-deflection characteristics of the external springs have some nonlinearity whereas they have been modeled as linear springs with a mean stiffness value. Since the mean stiffness values were obtained from the force-deflection curves of the springs, the overall force output is close to the experimentally obtained values but the shape of the two responses are slightly different. Similar to the unloaded case, a Fourier analysis of the experimental and modeled time domain force responses is performed and their spectral content is compared (see Figure 11). Despite the simplicity of the model, it accurately describes the first order component of the force response. However, the second order response is underestimated for all the springs.

Finally, the variation in energy output of the actuator with external spring stiffness is studied. An estimate of the energy output is obtained using the formula

$$E_o = \frac{1}{2}\left(\frac{(\frac{1}{2}F_{pkpk})^2}{k_{spring}}\right). \tag{28}$$

Figure 12 shows the energy output of the actuator as a function of the effective stiffness ratio defined as

$$k_{eff} = \frac{k_{spring}}{k_a}G^2, \tag{29}$$

where G is the kinematic gain given by the ratio of areas of the larger drive piston to the smaller driven piston, k_{spring} is the external spring stiffness, and k_a is the stiffness of the Terfenol-D rod. The energy output is maximum around the stiffness match region for both the experimental and modeled responses.

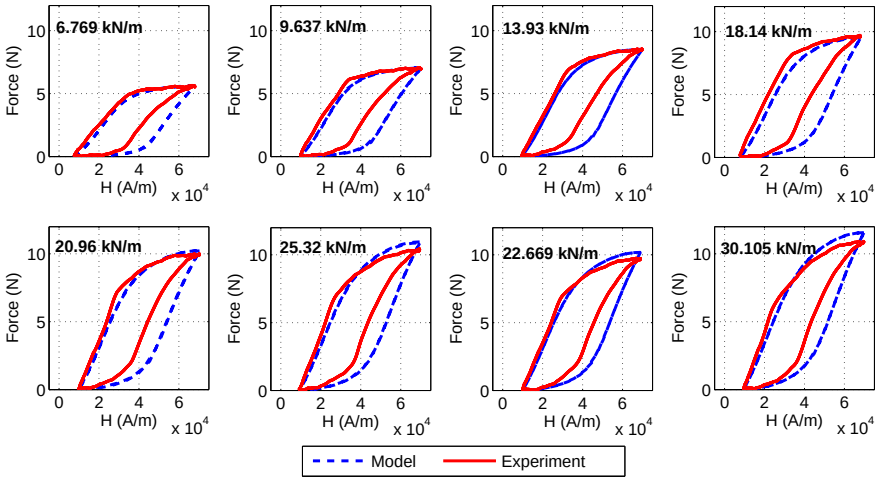

Figure 10. Force-field loops for different stiffnesses.

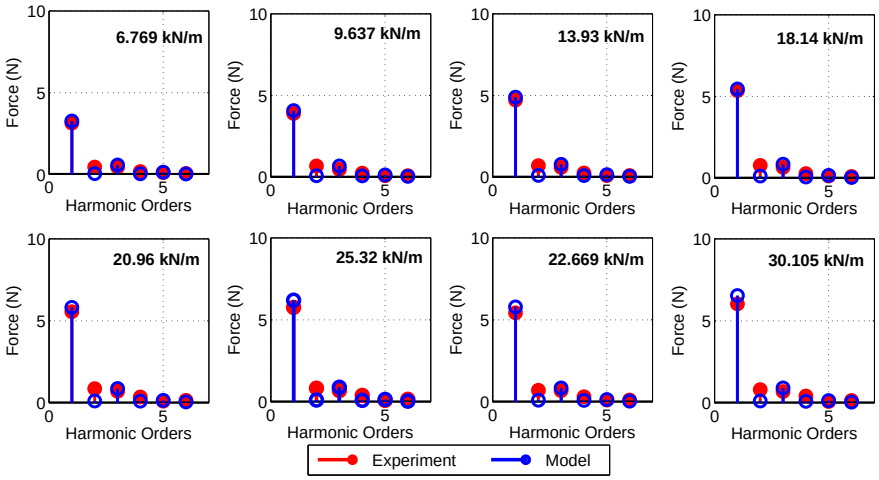

Figure 11. Output force orders.

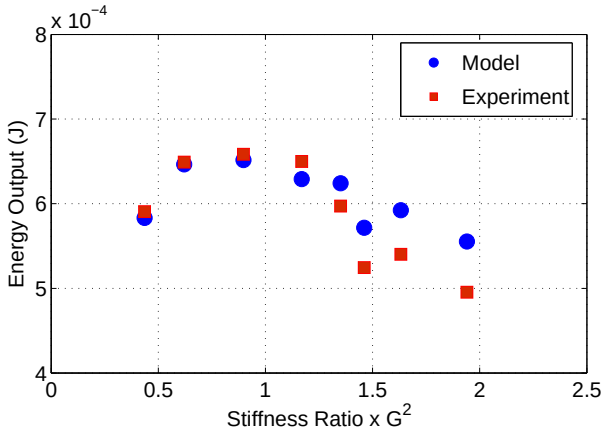

Figure 12. Variation of actuator energy output with load spring stiffness.

8. CONCLUDING REMARKS

A nonlinear model describing magnetic and vibratory dynamics of a hydraulically-amplified magnetostrictive actuator is presented. Due to the significant effect on performance of friction in the rubber seals, the LuGre model is implemented in combination with the vibratory equations. The actuator was tested in mechanically unloaded and loaded conditions; the external loading is applied with springs of different stiffness. In the unloaded condition, the model predicts the displacement-field loops accurately up to 500 Hz. The nonlinearity in the response is also described with sufficient accuracy in terms of the higher order components. In the loaded condition, the model accurately describes the first-order force response but underestimates the second-order force components. An energy analysis shows that the maximum energy delivered by the actuator to the load is around the stiffness match region, as expected theoretically.

ACKNOWLEDGMENTS

Support for this work comes from the member organizations of the Smart Vehicle Concepts Center (www.SmartVehicleCenter.org), the National Science Foundation Industry/University Cooperative Research Program (I/UCRC), and the Smart Vehicle Concepts Graduate Fellowship Program.

REFERENCES

[1] Lee, Y. and Lee, C., "Dynamic analysis and control of an active engine mount system," in [*Proc Instn Mech Engrs Part D: J Automobile Engineering*], **216**, 921–931 (2002).

[2] Matsuoka, H., Mikasa, T., and Nemoto, H., "Nv countermeasure technology for a cylinder-on-demand engine - development of active control engine mount," *SAE* (2004-01-0413) (2004).

[3] Ushijima, T. and Kumakawa, S., "Active engine mount with piezo-actuator for vibration control," *SAE* (930201) (1993).

[4] Shibayama, T., Ito, K., Gami, T., Oku, T., Nakajima, Z., and Ichikawa, A., "Active engine mount for a large amplitude of engine vibration," *SAE* (951298) (1995).

[5] Yoon, H.-S., Washington, G., Eyabi, P., Radhamohan, M., Woodard, S. W., and Dayton, R., "A millimeter-stroke piezoelectric hybrid actuator using hydraulic displacement amplification mechanism," *IEEE International Symposium on Industrial Electronics* **4**, 2809–2813 (July 2006).

[6] Giurgiutiu, V., Rogers, C. A., and Rusovici, R., "Solid-State Actuation of Rotor Blade Servo-Flap for Active Vibration Control," *Journal of Intelligent Material Systems and Structures* **7**(2), 192–202 (1996).

[7] Chakrabarti, S. and Dapino, M. J., "Design and modeling of a hydraulically amplified magnetostrictive actuator for automotive engine mounts," *Industrial and Commercial Applications of Smart Structures Technologies* **7290**(1), 72900D, SPIE (2009).

[8] S. Chakrabarti and M.J. Dapino, "Modeling of a displacement amplified actuator for active mounts," *Proceedings ASME Conference on Smart Materials, Adaptive Structures and Intelligent Systems*, SMASIS09-1411, Ellicott City, Maryland, (2008).

[9] Dapino, M., Smith, R., and Flatau, A., "Structural magnetic strain model for magnetostrictive transducers," *IEEE Transactions on Magnetics* **36**, 545–556 (2000).

[10] Huang, W., Wang, B., Cao, S., Sun, Y., Weng, L., and Chen, H., "Dynamic strain model with eddy current effects for giant magnetostrictive transducer," *IEEE Transactions on Magnetics* **43**, 1381–1384 (2007).

[11] Sarawate, N. and Dapino, M. J., "A dynamic actuation model for magnetostrictive materials," *Smart Materials and Structures* **17** (2008).

[12] Knoepfel, H. E., [*Magnetic Fields: A Comprehensive Theoretical Treatise for Practical Use*], John Wiley and Sons, New York, NY (2000).

[13] Jiles, D. and Atherton, D., "Theory of ferromagnetic hysteresis," *Journal of Magnetism and Magnetic Materials* **61**(1-2), 48 – 60 (1986).

[14] Dapino, M., Smith, R., Calkins, F., and Flatau, A., "A coupled magnetomechanical model for magnetostrictive transducers and its application to villari-effect sensors," *Journal of Intelligent Material Systems and Structures* **13**(11), 737–748 (2002).

[15] Olsson, H., Astrom, K. J., de Wit, C. C., Gafvert, M., and Lischinsky, P., "Friction models and friction compensation," *Eur. J. Control* **4**(3), 176–195 (1998).